Title: Investigation of flame radiation sampling and temperature measurement through light field camera

Authors: Jun Sun[1],

Md. Moinul Hossain[2],

Chuanlong Xu[1*],

Biao Zhang[1],

Yudong Liu[1]

Shimin Wang[1],

[1]School of Energy & Environment

Southeast University

No. 2 Sipailou Road, Nanjing, 210096, P.R. China

[2]School of Engineering and Digital Arts

The University of Kent,

Canterbury, Kent CT2 7NT, UK

E-mails: j_ustdoit@126.com, m.hossain@kent.ac.uk, chuanlongxu@seu.edu.cn*,
zhangbiao@seu.edu.cn, yudong.liu@seu.edu.cn, smwang@seu.edu.cn

*Corresponding author: Tel: 86-025-83794395

Abstract

Different light field cameras (traditional and focused) are considered for the flame temperature measurement in recent years. But it is crucial to investigate which light field camera can provide better reconstruction accuracy for the flame temperature. In this study, numerical simulations were carried out to investigate the reconstruction accuracy of the flame temperature for the different light field cameras. The effects of flame radiation sampling of the light field cameras were described and evaluated. A novel concept of sampling region and sampling angle of the light field camera was proposed to assess the directional accuracy of the sampled rays of each pixel on the photosensor. It has been observed that the traditional light field camera sampled more rays for each pixel, hence the sampled rays of each pixel are approached less accurately from a single direction. The representative sampled ray was defined to obtain the direction of flame radiation. The radiation intensity of each pixel was calculated and indicated that the traditional light field camera sampled less radiation information than the focused light field camera. A non-negative least square (NNLS) algorithm was used to reconstruct the flame temperature. The reconstruction accuracy was also evaluated for the different distances from microlens array (MLA) to the photosensor. The results obtained from the simulations suggested that the focused light field camera performed better in comparison to the traditional light field camera. Experiments were also carried out to reconstruct the temperature distribution of ethylene diffusion flames based on the light field imaging, and to validate the proposed model.

Keywords—Focused light field camera; Traditional light field camera; Radiation sampling; 3-D reconstruction; Flame temperature

1. Introduction

Flame temperature and its distributions are the most important parameter closely linked to the furnace safety, combustion efficiency, and pollutant emissions formation process. To improve understanding of the combustion phenomena and make consequent optimization of the combustion process, three-dimensional (3-D) distributions of the flame temperature have become increasingly important to combustion engineers [1-3]. Recently, the light field camera originated from the light slab parameterization [4] is proved a promising sensing device for the 3-D flame temperature measurement [5] where the radiation intensity and direction of ray can simultaneously be recorded through a single light field camera in a single exposure [6-8]. As a light field sampling detector, the light field camera is divided into focused and traditional light field camera due to different distances from MLA to the photosensor [9]. In traditional light field camera, the MLA is focused on the main lens. In contrast, a plane behind the main lens is focused by the MLA in the focused light field camera. But both of them can be used to sample the flame radiation as well as to reconstruct the 3-D flame temperature [5]. However, it is significantly important to investigate which light field camera can provide better reconstruction accuracy and reliability for the flame temperature measurement. Because the accurate and reliable 3-D measurements of the flame temperature are crucial for improving the combustion efficiency and controlling the combustion products such as NO_x and particulate matter [10**,** 11].

Over the past few years, a number of techniques have been developed to reconstruct the 3-D flame temperature [1-2, 12-24]. They are mainly categorized into laser-based diagnostics [1, 2, 12], acoustic techniques [13] and image-based techniques [14-**Error! Reference source not found.**]. The sampled signal (image or spectrum) such as hyperspectral absorption spectroscopy [2] rely on the participation of laser in the laser-based techniques. Although the laser-based techniques [1- 2, 12] are effective in combustion studies, they are mainly applied in the laboratory due to the complex setup and high-cost of the system. In acoustic techniques, the signal (acoustic propagation speed) is sampled by acoustic transmitters and receivers around the flame [13]. However, the spatial resolution of the sampled signal is very limited due to the number of the acoustic transmitters and receivers. In image-based techniques [14-20], mostly complementary metal-oxide-semiconductor (CMOS) or charge coupled device (CCD) cameras are utilized to capture flame images and to sample the flame radiation. The flame temperature is then reconstructed using optical emission tomographic techniques [e.g., filtered back-projection (FBP) and algebraic reconstruction techniques (ART)] [15]) and inverse algorithms (e.g., Least square QR-factorization (LSQR) [5], Truncated singular value decomposition, (TSVD) [16]). The image-based techniques do not require imposing external signal (laser)

and hence they are simple in the sampling system in comparison to the laser-based and the acoustic techniques. In the image-based techniques, the temporal and spatial resolution of the sampled flame radiation can be improved by integrating highly configured CCD or CMOS sensor. However, as the image-based techniques use the conventional cameras [14-**Error! Reference source not found.**], they cannot directly sample the 3-D flame radiation and thus limited to two-dimensional (2-D) images. So, the image-based technique with a single conventional camera can only be applied to the flame with a high level of axis symmetry [14]. For unstable and highly turbulent flames, the multi-cameras system is required [15-**Error! Reference source not found.**] and yet their installation is too complex. To address the above issues, recently proposed a single focused light field camera system to reconstruct the 3-D flame temperature [5, 24]. Niu et al. [24] also utilized the light-field image of ethylene diffusion flame with the Al_2O_3 particle to reconstruct the temperature field and radiative properties of the flame. However, in their studies, the effects of flame radiation sampling and distances from MLA to the photosensor were not considered and which light field camera is more suitable for the flame temperature measurement was not investigated [5, 24].

Except for the flame temperature measurement, the light field cameras were used in various studies such as face recognition and 3-D dose reconstruction [25-29]. Studies were also undertaken [30-32] to investigate the resolution of refocusing images in the field of image rendering where the authors clearly addressed that the different light field cameras have different ratios of spatial to directional resolutions [30-31]. Georgiev et al. [30] also addressed that it is advantageous to use the focused light field camera for improving the resolution of resultant refocusing images, particularly for the image rendering process. Therefore, different light field cameras with different ratios of spatial to directional resolutions will lead to different sampling patterns of the flame radiation which can affect the reconstruction accuracy of the flame temperature.

Measurement of the flame temperature using the light field cameras would basically be different in three aspects from the image rendering. Firstly, the light field distributions of targets are different. For the image rendering, the targets of the light field camera are generally not transparent and self-radiative such as trees, houses and people [30-32]. But a flame is translucent and self-radiative [8], and the flame image sampled by the light field camera is generated by the integral of all the radiation along the propagation path instead of the flame surface. Where each sampled ray not only samples the radiation information of corresponding object point on the surface but also samples the radiation information of all object points along the propagation path, and each sampled ray includes the radiation information from more than one objects point. Therefore, it is difficult to determine the radiation information of all the object points along the propagation path of one sampled ray and hence more sampled rays are required for an in-depth understanding the internal

structure of the flame. Secondly, the purpose of the application is different. The light field cameras are used to reconstruct the flame temperature accurately instead of rendering high-resolution images. Even though the resolution of refocused images is high, the reconstruction accuracy may not be high. The lower resolution of the refocused flame image would also be acceptable if the flame temperature reconstructed with higher accuracy. Finally, for the temperature measurement and the image rendering, potential influence factors such as ratios of spatial to directional resolutions would be different. The measurement accuracy of the flame temperature is also related to other factors such as the number of sampled rays of each pixel on the photosensor and the distribution of sampled rays. However, it is very scarce to find the studies on the radiation sampling of the light field cameras with distinct distances from MLA to the photosensor in the field of flame temperature measurement. Therefore, there is a need of investigating the radiation sampling of the different light field cameras along with distances from MLA to the photosensor for the flame temperature measurement.

The main contribution of this study is to investigate the effects of the radiation sampling of the different light field cameras with different distances from MLA to the photosensor for the flame temperature measurement. An innovative concept of sampling region (*SR*), sampling angle (*SA*) of the light field camera is proposed to characterize the flame radiation sampling. A radiative imaging technique is also modeled for the flame temperature measurement. The distribution of the representative sampled rays of the light field camera is analyzed. Numerical simulations are performed to reconstruct the axisymmetric flame temperature using a non-negative least square (NNLS) algorithm [33]. Results obtained from the numerical simulations are presented and discussed. Experiments are also carried out to validate the proposed NNLS algorithm for realistic flames.

Nomenclature

d_p	Side length of each pixel [mm]
N_m	Number of pixels on the diameter of each sub-image
N_s	Number of microlenses in a row or column
ω	Magnifying factor of the aperture
f_m	Focal length of the microlens [mm]
d_m	Diameter of each microlens [mm]
f	Focal length of the main lens [mm]

d	Diameter of each sub-image [mm]
D	Diameter of the main lens [mm]
D_o	Diameter of aperture [mm]
L_{ix}	Distance from intermediate image plane to MLA [mm]
L_{ux}	Distance from main lens plane to MLA [mm]
L_{xp}	Distance from MLA to the photosensor [mm]
L_{ou}	Distance from object plane to main lens plane [mm]
b	Beam of sampled rays
SR	Sampling region [mm]
$SAPU$	Sampling angle per unit [°/mm]
SA	Sampling angle [°]
SNR	The signal-to-noise ratio
T_o	True value of flame temperature [K]
T_r	Reconstructed value of flame temperature [K]
R	Radius of the flame [mm]
Z	Height of the flame [mm]
Z_r	Axial direction of the flame
R_r	Radial direction of the flame
C_r	Circumferential direction of the flame
$\boldsymbol{I}_p$	Vector comprised of the radiative intensity of each pixel on the photosensor [W/m^2/sr]
$\boldsymbol{I}_b$	Vector comprised of the blackbody radiation of each voxel of the flame [W/m^2/sr]
$\boldsymbol{A}$	Coefficient matrix related to the optical thickness
N_i	Noise value of the i-th pixel of the flame image on the photosensor [W/m^2/sr]
k	Number of the pixels of the flame image on the photosensor.
σ	Stefan–Boltzmann constant [5.670373 × 10^{-8} W/m^2/K^4]
δ_T	Relative error of the reconstructed temperature of each voxel [%]
Δ_T	Mean value of the relative error δ_T of the reconstructed temperature of flame voxels [%]

2. Radiation sampling

2.1 Parameter settings of the light field camera

To investigate the radiation sampling of the different light field cameras, numerical simulations are carried out. Figure 1 shows the structure of the light field cameras applied for the radiation sampling of a flame. The light field cameras have real components of MLA, photosensor and main lens. The main lens has a focal length f = 50 mm. The MLA with $N_s \times N_s$ microlenses is assembled in front of photosensor with a distance of L_{xp} and each microlens covers $N_m \times N_m$ pixels. Each pixel has the size of d_p. For the traditional light field camera, the distance of L_{xp} is equal to the focal length of microlens (i.e., $L_{xp} = f_m$), and yet $L_{xp} \neq f_m$ for the focused light field camera. Based on the distance of L_{xp}, object plane and intermediate image plane are defined for the both light field cameras to analyze the radiation sampling. For the traditional light field camera, the object plane is the conjugate plane of MLA for the main lens whereas for the focused light field camera it is the conjugate plane of the intermediate image plane for the main lens. The flame center is located in the object plane of the light field camera to ensure the light field camera focuses the flame. The intermediate image plane is the conjugate plane of the photosensor for the microlens in the focused light field camera. There is no intermediate image plane in the traditional light field camera.

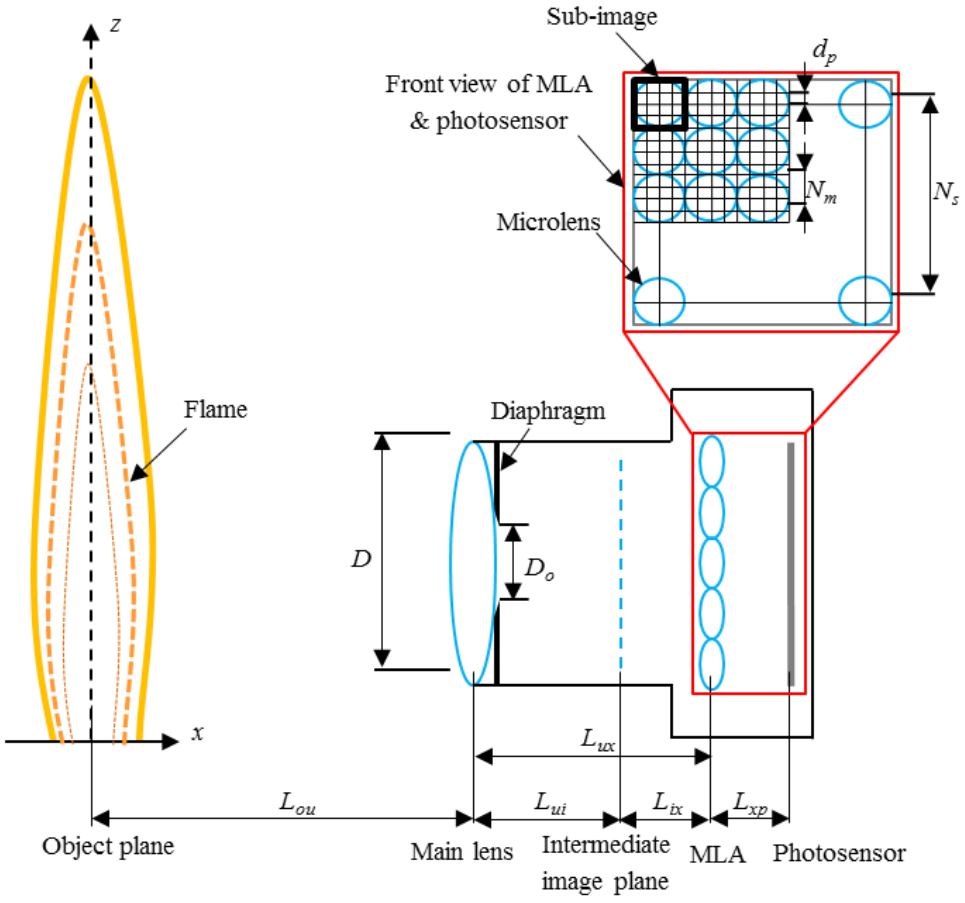

Fig. 1. The structure of the light field camera applied for the radiation sampling of a flame.

The input parameters (d_p, N_m, N_s, f_m and f) used in the simulation are selected from the commercial focused light field camera of Raytrix (R29) and the parameters are listed in Table 1. Variation of distances from MLA to the photosensor (L_{xp}) satisfies the Eq. (1) so that each point on the virtual object point is imaged by at least two different microlenses [34]. For the traditional light field camera, L_{xp} is set to $1.0f_m$. Without loss of generality, eight different distances (i.e., L_{xp} = $0.6f_m$, $0.7f_m$, $0.8f_m$, $0.9f_m$, $1.1f_m$, $1.2f_m$, $1.3f_m$, and $1.4f_m$) from MLA to the photosensor are chosen for the focused light field camera.

$$\frac{1}{2} f_m < L_{xp} < \frac{3}{2} f_m \tag{1}$$

The distance (L_{ux}) between the main lens and the MLA is calculated using Eq. (2). The constant 1.11 is the ratio of the image distance to the focal length of the main lens, named as imaging factor in this study. It is mainly selected based on the experiment described in Ref. [5]. The distance (L_{ix}) between the virtual image and the MLA is determined based on the conjugate relation of the microlens and expressed by Eq. (3). The objective distance (L_{ou}) is also calculated based on the conjugate relation of the main lens and defined by Eq. (4). In this study, sub-image (black square box in Fig.1) refers to a group of pixels that covered by each microlens. A factor (ω) is introduced in Eq. (5) to make sure two arbitrary sub-images have at least one pixel that cannot sample the radiation on their boundary. The aperture diameters (D_o and D) are set based on matching F-number of the microlens and the main lens [6] and then calculated by the Eq. (5). The diameter (d_m) of the microlens is determined by Eq. (6) as the images covered by the microlenses are maximal in size without overlapping.

$$L_{ux} = 1.11 \times f + 1/(1/f_m - 1/L_{xp}) \tag{2}$$

$$L_{ix} = 1/(1/f_m - 1/L_{xp}) \tag{3}$$

$$L_{ou} = \begin{cases} 1/(1/f - 1/L_{ux}) & L_{xp} = f_m \\ 1/[1/f - 1/(L_{ux} - L_{ix})] & L_{xp} \neq f_m \end{cases} \tag{4}$$

$$D_o = \omega \times D = \omega \times \frac{L_{ux}}{L_{xp}} \times d = \omega \times \frac{L_{ux}}{L_{xp}} \times N_m \times d_p \tag{5}$$

$$d_m = D/(L_{ux} + L_{xp}) \times L_{xp} \tag{6}$$

Table 1. Parameters of the light field camera

d_p (mm)	N_m	N_s	f_m (mm)	f (mm)	L_{xp} ($\times f_m$)	L_{ux} (mm)	L_{ix} (mm)	L_{ou} (mm)	ω	D (mm)	D_o (mm)	d_m (mm)
0.008	12	60	0.6	50	0.6	54.6	-0.9	505	0.45	14.6	6.55	0.095
0.008	12	60	0.6	50	0.7	54.1	-1.4	505	0.55	12.4	6.80	0.095
0.008	12	60	0.6	50	0.8	53.1	-2.4	505	0.65	10.7	6.90	0.095
0.008	12	60	0.6	50	0.9	50.1	-5.4	505	0.75	8.9	6.68	0.095
0.008	12	60	0.6	50	1.0	55.5	0.0	505	0.85	8.9	7.55	0.095
0.008	12	60	0.6	50	1.1	62.1	6.6	505	0.75	9.0	6.77	0.095
0.008	12	60	0.6	50	1.2	59.1	3.6	505	0.65	7.9	5.12	0.095
0.008	12	60	0.6	50	1.3	58.1	2.6	505	0.55	7.2	3.93	0.095
0.008	12	60	0.6	50	1.4	57.6	2.1	505	0.45	6.6	2.96	0.095

2.2 Sampling region (SR) and sampling angle (SA)

In the light field camera, basically one single pixel represents a unit of sampling radiation and it is necessary to investigate the characteristics of the sampled radiation of the unit. Various rays of the flame radiation can be projected on the single unit from different directions. The intensity of the unit is the averaged radiation intensity of all the directions. The radiation intensity from a single direction is required to obtain for the flame temperature reconstruction [5, 24]. Therefore, the sampled radiation of the unit has to be determined from a single direction. It is worth mentioning that for the less number of sampled rays, the sampled radiation of the unit can be approached more accurately from a single direction in comparison to a large number of sampled rays. The sampled rays of the pixels on the photosensor are from the object plane inside the flame. For each pixel, the number of sampled rays depends on the (a) number of radiation points on the object plane, (b) a number of sampled rays from each radiation point. Therefore, the location of the sampled rays has to be determined to investigate the two parameters [(a) and (b)] on the object plane. To evaluate the two parameters, the sampling region and sampling angle/unit were defined and described.

Figure 2 shows a schematic diagram of the sampled rays of the light field cameras for a single pixel. To detect the location of the sampled rays inside the flame, the sampled rays of each pixel are traced from the photosensor to the object plane based on the geometrical optics described in Ref. [35]. Then the sampling

region (*SR*) is obtained to represent the region which emits rays of flame radiation on a single pixel. To explain the sampled rays of each pixel, three beams (b_1, b_2 and b_3) of rays are assigned and traced backwards from three uniformly distributed points [e.g. Points 1, 2 and 3, refer to Fig. 2(a)] for each pixel. Basically, the three beams represent the all sampled rays of each pixel. For the traditional light field camera, it can be seen that the beam is diverging from the main lens to the object plane, as shown in Fig. 2(a). Whereas for the focused light field camera, it is convergent from the main lens to the object plane, as shown in Fig. 2(b). This is due to fact that the conjugate points of the starting points (e.g. Points 1 and 8) are located on different planes for the microlens. In the traditional light field camera, the conjugate point (Point 5) of the starting point (Point 1) for the microlens are on the main lens plane [refer to Fig. 2(a)] and the beam b_1 from Point 5 is then diverged by the main lens. In the focused light field camera, the conjugate point (Point 9) of the starting point (Point 8) for microlens are on the intermediate image plane [refer to Fig. 2(b)] and the beam b_1 from Point 9 is then converged to Point 10 by the main lens. So the different light field cameras have different radiation sampling characteristics for the translucent flame.

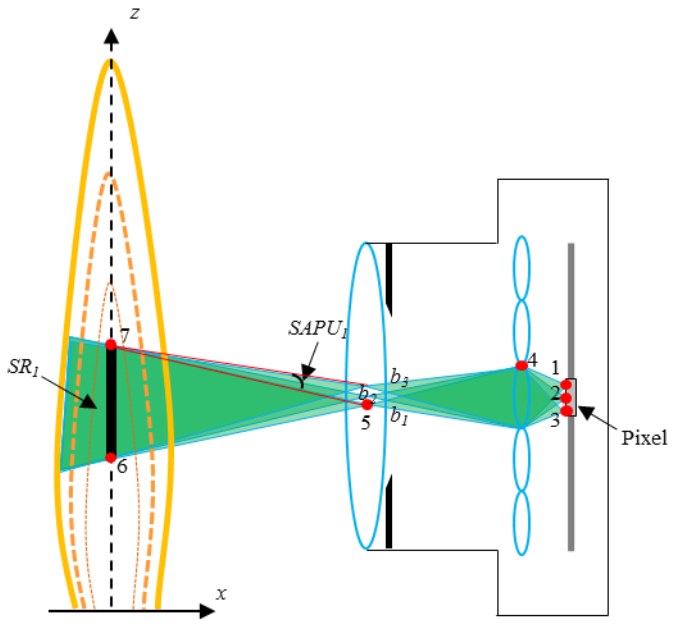

(a) $L_{xp} = f_m$ *(*Traditional light field camera)

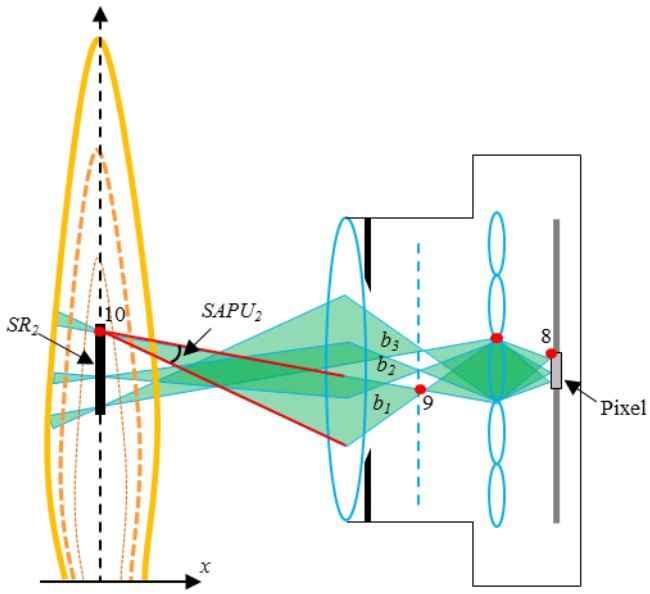

(b) $L_{xp} \neq f_m$ (Focused light field camera)

Fig. 2. Schematic of the sampled rays of a single pixel of the light field cameras.

Despite that, all the sampled rays of each pixel can be considered to comprise a series of beams (refer to Fig. 3) from the radiation points on the *SR* such as Points 6 and 7, as shown in Fig. 3. This figure further illustrates the sampled beams of rays on the *SR* for the 3-D [Fig.3 (a)] and 2-D cases [Fig.3 (b)] without loss of generalization. In order to evaluate the number of sampled rays of each pixel, the sampling angle/unit (*SAPU)* is defined as a solid angle of the beam from the radiation point on the *SR*. It is assumed that the distributions of sampled rays are uniform in the 3-D space. In other words, the number of rays in each direction is constant from an arbitrary radiation point in the 3-D space. The number of sampled rays of a single radiation point is in proportion to the *SAPU*. The greater *SAPU* means more sampled rays from the single radiation point. The number of radiation points on the *SR* is in proportion to the area (3-D case) or length (2-D case) of the *SR*. The total number of rays on the *SR* is then evaluated by the product of *SR* and *SAPU*. The product of *SR* and *SAPU* is defined as a sampling angle (*SA*) in this study. The total number of sampled rays of each pixel in *SR* is in proportion to the *SA*. The smaller *SA* is the less number of sampled rays of each pixel and thus the sampled rays of each pixel are accurately approached from a single direction. It means that the direction of the sampled rays for each pixel in the light field camera with the smaller *SA* can be more accurate.

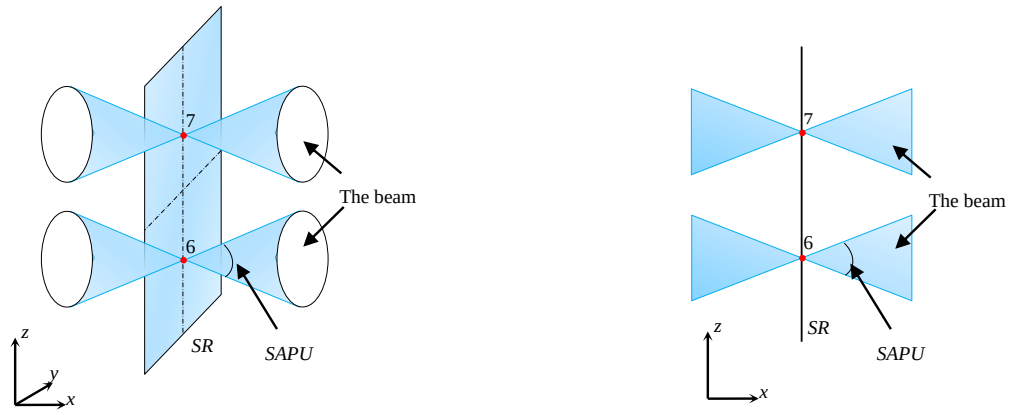

(a) 3-D case (b) 2-D case

Fig. 3. Schematic of the sampling region (*SR*) and the sampling angle/unit (*SAPU*).

For the 2-D case, the *SR* can be expressed by Eqs. (7) - (8) for the both light field cameras. The *SR* can also be generalized for the 3-D case by converting d_m and d_p by Eqs. (7) - (8) into the areas of the microlens and pixel. Similar to the *SR*, the *SAPU* of the pixels can be expressed by Eqs. (9) - (10) in the 2-D case. Eq. (9) is for the traditional light field camera, and Eq. (10) is for the focused light field camera. The *SAPU* can be generalized for the 3-D case by calculating the solid angle of the *SAPU*.

$$SR_1 = L_{ou} d_m / L_{ux} \tag{7}$$

$$SR_2 = L_{ou} L_{ix} d_p / L_{xp} / L_{ui} \tag{8}$$

$$SAPU_1 = \arctan\left(d_p L_{ux} / L_{xp} / L_{ou} \right) \tag{9}$$

$$SAPU_2 = \arctan\left(d_m L_{ui} / L_{ix} / L_{ou} \right) \tag{10}$$

$$SA = SR \times SAPU \tag{11}$$

The variation of *SR* with the different distances of L_{xp} is shown in Fig. 4. From this figure, it can be seen that the *SR* increases and then decreases with increasing of L_{xp}. The peak is obtained at $L_{xp} = 1.0 f_m$, indicating that the traditional light field camera provides the greater *SR* compared to the focused light field camera, and so has the lower spatial resolution.

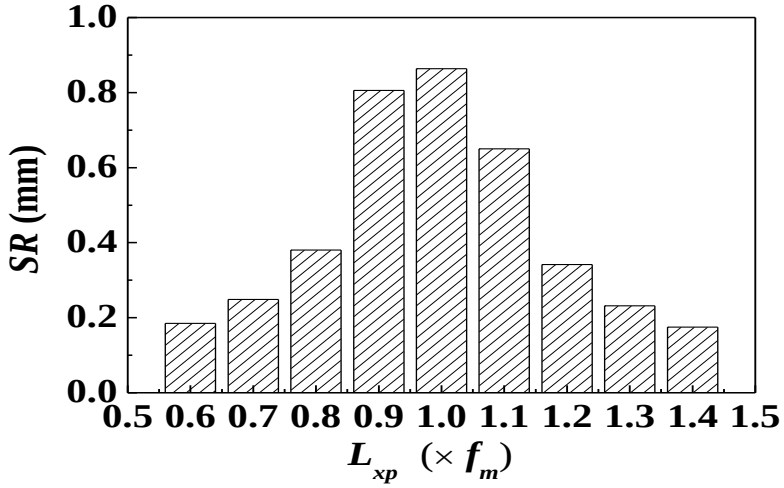

Fig. 4. The variation of *SR* with different L_{xp}.

Figure 5(a) shows the variation of *SAPU* with the distances of L_{xp}. It can be seen that the *SAPU* firstly decreases and then increases with increasing L_{xp} and the lowest is at L_{xp} =1.1f_m. This indicates that the traditional light field camera provides the lowest *SAPU* and so has the least number of sampled rays of a single point (e.g. Point 10) on the *SR*. To investigate the total number of sampled rays of each pixel with L_{xp}, the variation of *SA* with the distances of L_{xp} are then calculated and illustrated in Fig. 5 (b). From this figure, it has been observed that the *SA* decreases with the increasing of L_{xp}. As a consequence, for each pixel, the number of sampled rays decreases with the increasing of L_{xp} and the directional accuracy of the sampled rays' increases with the increasing of L_{xp}. The focused light field camera with L_{xp} =1.4f_m provides the least number of sampled rays and hence the sampled rays of each pixel are approached from a single direction more accurately. Consequently, it is more advantageous for the flame temperature reconstruction.

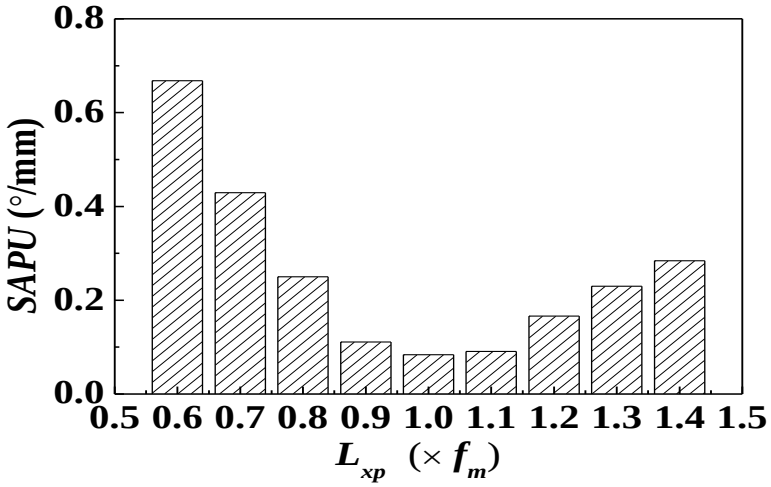

(a) Sampling angle/unit

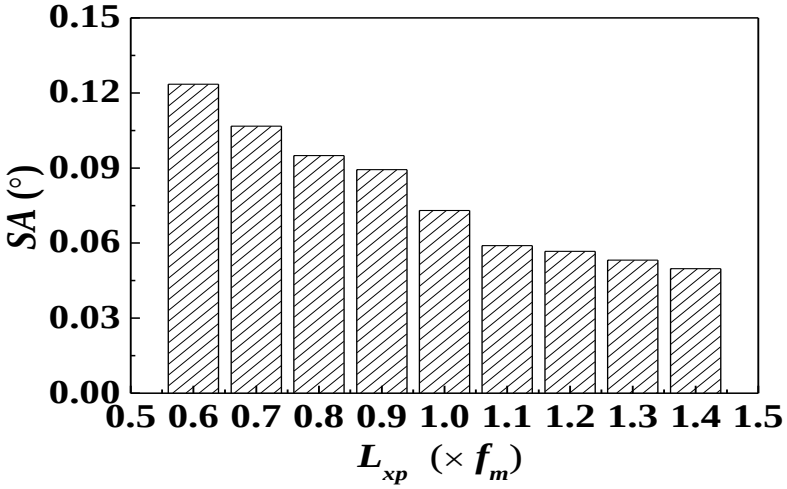

(b) Sampling angle

Fig. 5. The variation of *SAPU* and *SA* with different L_{xp}.

2.3 Representative sampled rays

As described in the previous section, the sampled rays projecting on a single pixel have to be determined from a single direction. In the conventional CMOS or CCD cameras, the principal ray (i.e., the ray crossed the center of the main lens) is considered as the direction of the sampled radiation of the pixel. In the light field cameras, the direction of the sampled radiation of the pixel is not the same with the conventional cameras.

In this study, a representative sampled ray is defined to describe the direction of the sampled radiation of the pixel for the following two cases;

Case 1: *The sampled rays of the pixel are from the whole microlens:* As shown in Fig. 6, all the sampled rays (red polygon) of the central pixel are from the whole microlens and the main lens aperture. So, the ray crossed the center of the microlens and the center of the pixel is defined as the representative sampled ray (refer to the enlarged view of Fig.6).

Case 2: *The sampled rays of the pixel are not from the whole microlens:* All the sampled rays (green polygon) of the edge pixel are not from the whole microlens but from a partial region (e.g. the region between Points *a* - *b*) of the microlens as shown in Fig. 6. The rays marked by grey polygon cannot be sampled because of the diaphragm. In this case, the ray crossed the center (e.g. Point *c*) of the partial region and the center of the pixel is defined as the representative sampled ray.

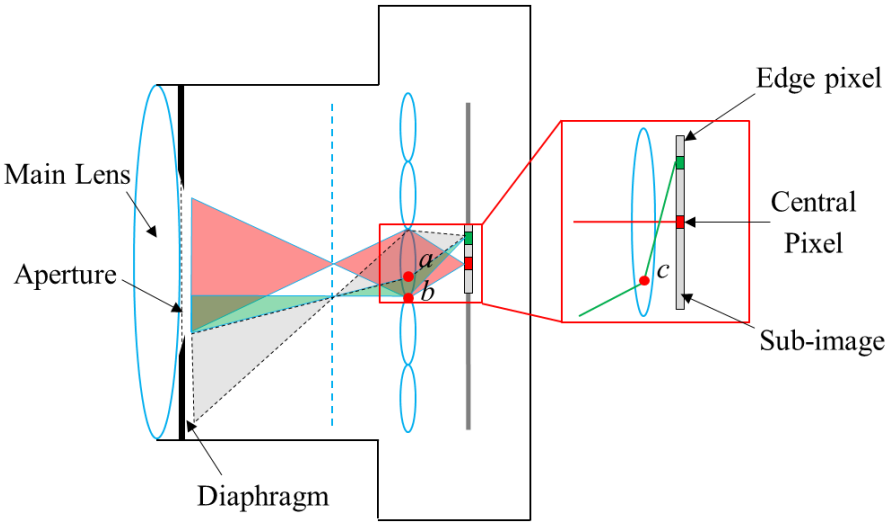

Fig. 6. The schematic of the representative sampled ray of the pixel in the sub-image.

By this way, the radiation sampling of the whole flame can be characterized by all representative sampled rays with known intensity. The distribution of the representative sampled rays reflects the overall sampling characteristics of the light field camera. The distribution of the representative sampled rays for the different light field cameras is investigated based on the input parameters as listed in Table 1. Figure 7 shows the distribution of the representative sampled rays in the *x*-*z* directions. Figure 7 (b) illustrates the schematic of the distribution of the representative sampled rays. In Fig .7 (b), the green rectangle is from 10 mm to 18 mm in the *z*-axis and from -8 mm to 8 mm in the *x*-axis and it represents a flame region of the light field camera.

In Fig. 7 (a) and (c) - (j), the red horizontal lines depict the representative sampled rays of the pixels covered by the two adjacent microlenses. The center of each representative sampled ray is on the object plane (i. e., $x = 0$ *mm*). For each $L_{xp,}$ only twenty representative sampled rays are selected and plotted in the figure and the other representative sampled rays have the similar distribution along the *z*-axis. It has been found that for the focused light field camera, the uniformity of the representative sampled rays is almost similar at $L_{xp} > f_m$ and $L_{xp} < f_m$ except for the $L_{xp} = 1.1f_m$. In contrast, the representative sampled rays are much non-uniform for the traditional light field camera ($L_{xp} = 1.0f_m$) compared to the focused light field camera. Because the traditional light field camera has a least spatial resolution [27] and thus the representative sampled rays are emitted from less number of points [the intersection points of the rays on the virtual focal plane, such as red point in Fig 8 (e)]. Therefore, the effective radiation information of the flame obtained by the traditional light field camera is less compared to the focused light field camera. Also, the distribution of representative sampled rays by the traditional light field camera is disadvantageous for the flame radiation sampling.

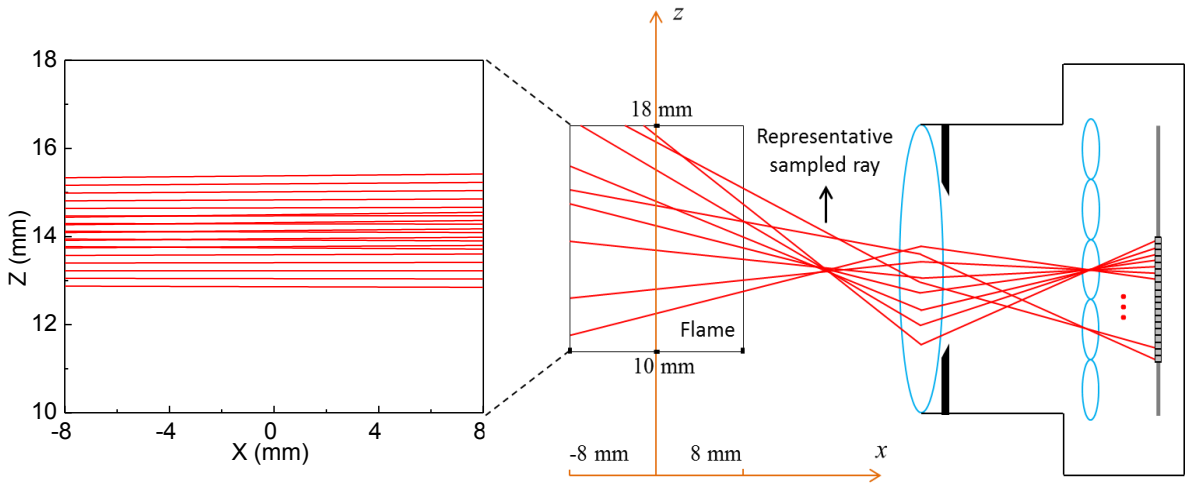

(a) $L_{xp} = 0.6f_m$

(b) Schematic of the distribution of the representative sampled rays

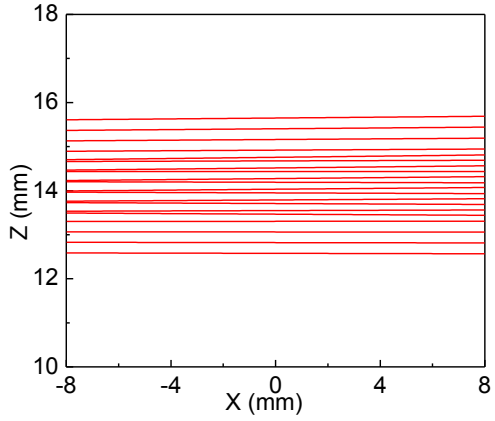

(c) L_{xp} =0.7f_m

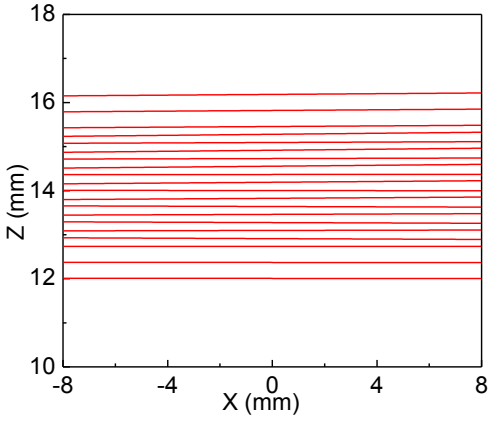

(d) L_{xp} =0.8f_m

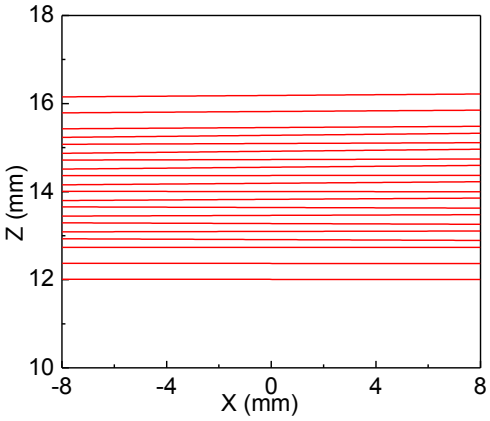

(e) L_{xp} =0.9f_m

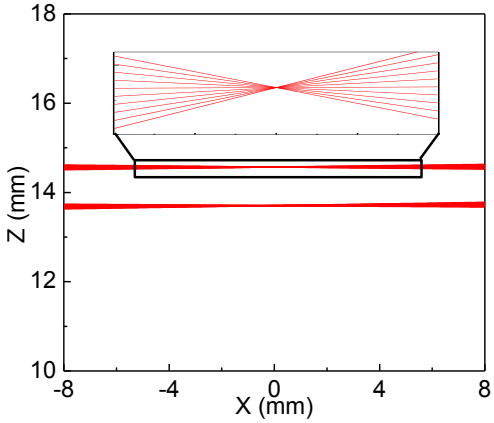

(f) L_{xp} =1.0f_m

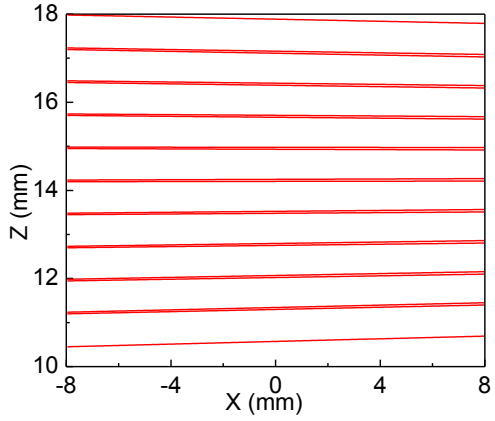

(g) L_{xp} =1.1f_m

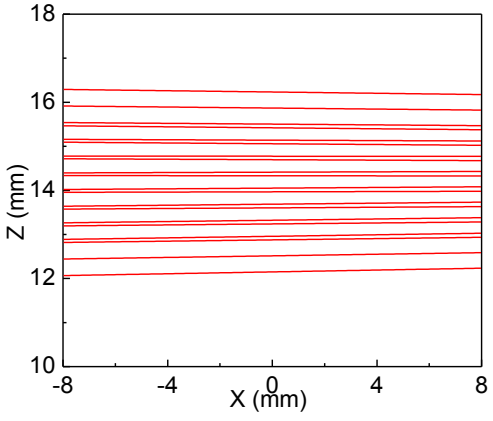

(h) L_{xp} =1.2f_m

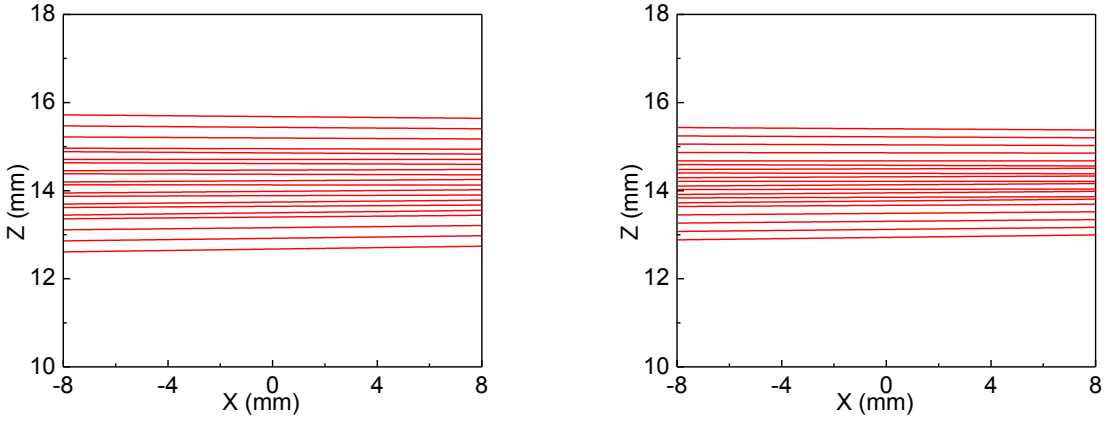

(i) L_{xp} =1.3f_m **(j) L_{xp} =1.4f_m**

Fig. 7. The distributions of the representative sampled rays for the different L_{xp}.

3. Methodology

In order to investigate the reconstruction accuracy of the flame temperature, numerical simulations are carried out for the different light field cameras by varying distances from MLA to the photosensor. In this study, a cylindrical flame is considered for the numerical simulation where the boundaries of the flame are assumed as transparent. The radius R and height Z of the cylindrical flame are set 8 mm and 30 mm, respectively based on the size of the photosensor. The flame absorption coefficient of 3 m^{-1} [29, 36, 37] is considered, and the scattering effect is not considered in this study because the scattering capacity of soot particles in the flame is much smaller than the absorption capacity [38]. In this simulation, flame geometry, the spectral and spatial dependency of the absorption coefficients of the flame has been simplified to enable the effective analysis of the optical effects such as sampling angle, distributions of the representative sampled rays for the temperature reconstruction. The whole flame is divided into 100 (10×10×1) voxels in the axial (Z_r), radial (R_r) and circumferential (C_r) directions. For the simulation, the axisymmetric temperature distributions T_0 is defined and it is assumed to be the function of z and r as given by Eq. (13). The temperature distribution is shown in Fig. 12(a). The input parameters for the different light field cameras and the flame are initialized and described in Section 2.1. The size of the flame should satisfy the Eq. (12) to ensure the size of the light field flame image is less than that of the size of the photosensor.

$$\begin{cases} \max\{2R, Z\} < \dfrac{L_{ou}}{L_{ux}} dN_s & \left(L_{xp} = f_m\right) \\ \max\{2R, Z\} < \dfrac{L_{ou}}{L_{ui}} dN_s & \left(L_{xp} \neq f_m\right) \end{cases} \tag{12}$$

$$T_o(r, z) = 1200 \exp\left\{-\left[3\left(\frac{r^2}{R^2} + \frac{z^2}{Z^2}\right) - 0.9\right]^2\right\} + 900 \quad (K) \tag{13}$$

where R and Z are the radius and height of the cylindrical flame, respectively. N_s is the number of microlenses (or sub-images) in a row or column and d is the diameter of each sub-image. So $d \times N_s$ is equal to the side length of the sensor. r and z are the radials and axial coordinates along axial (Z_r), radial (R_r) directions of the cylindrical flame. In the simulation, it is required to calculate the intensity of the sampled rays to acquire the flame intensity of each pixel. The sampled rays of each pixel are generated and traced from the photosensor to the flame.

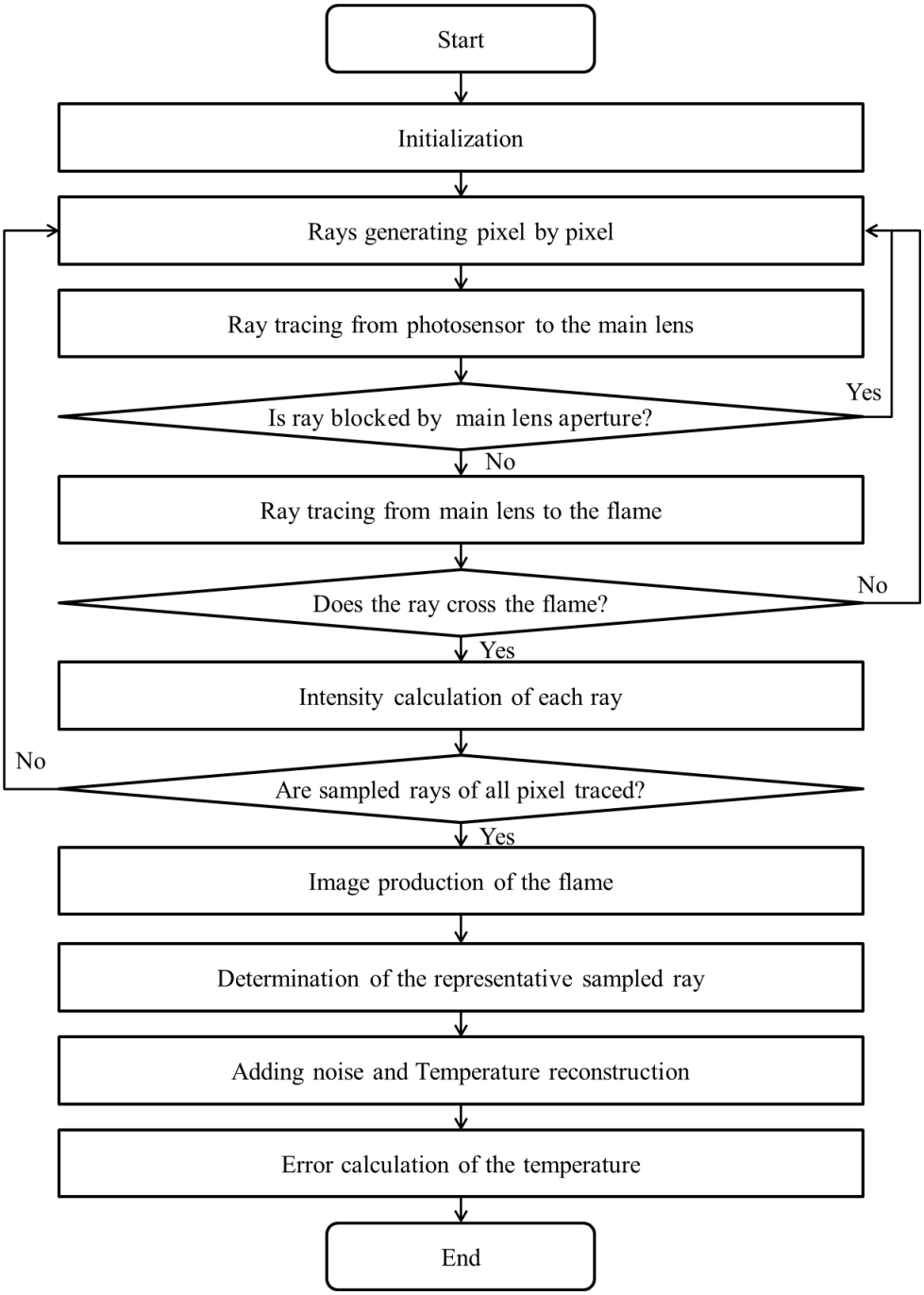

Fig. 8. Flow chart of the numerical simulation.

The implementation of the numerical simulation of the flame image formation and temperature reconstruction are performed according to the following procedure:

Step 1. *Rays generating:* To generate a ray of each pixel, two points on the photosensor plane and the microlens plane are initially defined. For instance, Points 1 and 4 in Fig. 2 are defined to obtain a ray. In this

way, all the points on the photosensor and the microlens plane are uniformly defined to obtain all the rays of each pixel.

Step 2. *Rays tracing:* The generated rays are then traced from the photosensor to the flame using thin lens equation as described in Ref. [35]. However, when tracing the rays from MLA to the main lens, some of the rays are blocked by the main lens aperture (refer to Fig. 6). These blocked rays cannot be used to determine the intensity of each pixel. But, the remaining rays passing through the main lens aperture are employed as sampled rays to calculate the intensity of each pixel. For the blocked rays, the ray tracing is stopped and the simulation starts to generate another ray of the pixel from **Step 1**.

Step 3. *Intensity calculation:* After tracing the ray from the photosensor to the flame, it is crucial to determine whether the traced ray crossed the flame or not. Flame radiation cannot be obtained if the ray does not cross the flame. Then the simulation starts to generate another ray on the pixel from **Step 1**. But if the ray crossed the flame, a radiative transfer equation can be applied to calculate the intensity of the sampled ray and expressed by Eq. (14) [5].

$$I_n = I_{bn}(1-\exp(1-\tau_n)) + \sum_{i=1}^{n-1}(\exp(-\sum_{j=i+1}^{n}\tau_j) - \exp(-\sum_{j=i}^{n}\tau_j))I_{bi} \tag{14}$$

where I_n is the radiative intensity of the ray passing through the flame. I_b and τ are the intensity of blackbody radiation and the optical thickness of the voxel, respectively.

Step 4. *Image formation:* If the generated rays of all pixels are not traced, the simulation starts to generate another ray using **Step 1**. When the generated rays of all pixels are traced, the intensity of the rays is then calculated. The intensity $\bar{I}$ of each pixel is achieved by averaging the intensities of the sampled rays of the pixel by applying Eq. (15). In this way, the intensity of the total number of pixels of the flame are obtained and the final light field image is formed. After that the image is converted to gray level and then normalized by minimum to the maximum intensity of each image in the range of 0 to 1.

$$\bar{I} = \frac{\sum_{i=1}^{m} I_i \cos\theta_i}{m} \tag{15}$$

where n is the number of the voxels of the flame and m is the number of sampled rays of the pixel. I_i is the radiative intensity of i-th ray of each pixel. θ_i denotes the angle between the i-th ray and the normal vector of the photosensor.

Step 5. *Determination of representative sampled ray:* After tracing all the rays of each pixel, the sampled rays of the pixel obtained only for the rays are passed through the main lens aperture. These sampled rays of each pixel covered a region on the corresponding microlens of the pixel. Then the ray crossed the center of the region covered by the sampled rays and the center of the pixel is defined as the representative sampled ray (refer to Fig. 6 in Section 2.3). The intensity of the representative sampled ray is regarded as the intensity of the pixel which was calculated in **Step 4**.

Step 6. *Temperature reconstruction:* A linear equation is derived for the representative sampled rays and expressed by Eq. (15). An inverse non-negative least square (NNLS) algorithm is applied to solve the Eq. (15) for the temperature reconstruction of the simulated flame. The detailed procedures of the NNLS algorithm can be found in Ref. [33]. For the inverse problem of the flame temperature reconstruction, the sampled flame radiation generally has noises caused by the measurement set-up. So the Gaussian noises with a signal-to-noise ratio (*SNR)* of 15dB and 20dB are added to the intensity of each pixel as measurement errors. In this study, the *SNR* is obtained by Eq. (17). The monochromatic intensity of the blackbody radiation I_{bi} of each voxel is then obtained by solving the Eq. (16) using the NNLS algorithm. Finally, the temperature T_i of each voxel is calculated by using Eq. (18) based on the Stefan–Boltzmann law [39].

$$\boldsymbol{I}_p = \boldsymbol{A}\boldsymbol{I}_b \tag{16}$$

$$SNR = 10\log_{10}\left[\frac{\sum_{i=1}^{k}\left(I_p^i\right)^2}{\sum_{i=1}^{k}\left(N_i\right)^2}\right] \tag{17}$$

$$T_i = (I_{bi}\pi/\sigma)^{\frac{1}{4}} \tag{18}$$

where I_p^i is the radiative intensity of the representative sampled ray of *i*th pixel of the flame image on the photosensor, $\boldsymbol{I}_p$ is the vector comprised of the radiative intensity of each pixel. $\boldsymbol{I}_b$ is the vector comprised of the blackbody radiation of all voxels. $\boldsymbol{A}$ is the coefficient matrix related to the optical thickness and it is determined by the Eq. (14). N_i is the noise value of the *i*th pixel of the flame image. k is the number of pixels of the flame image and σ is the Stefan–Boltzmann constant.

Step 7. *Relative error calculation:* To evaluate the reconstruction accuracy, the relative error Δ_T between the reconstructed temperature T_r and the true temperature T_o of each voxel is calculated by Eq. (19).

$$\Delta_T = \frac{|T_r - T_o|}{T_o} \times 100\% \quad (19)$$

The detailed flow chart of the numerical simulations of the flame temperature reconstruction is presented in Fig. 8.

4. Results and discussion

4.1 The simulated flame image

Figure 9 shows the simulated images of the flame obtained by light field camera with the different distances of L_{xp}. From Fig. 9, macroscopically the light field flame image looks like the image normally taken by a conventional camera, and yet they have some dark and bright sub-images. The dark pixel in the light field image means that the predetermined ray of the pixels does not pass through the flame and so no radiation is detected by the pixel of sub-image. On the contrary, the bright pixel receives the radiation from the flame. Obviously, the structure of the flame image of the focused light field camera is different from that of the traditional light field camera. In the edge of the flame image, the bright sub-images of the flame are mostly circular at $L_{xp} = 1.0\ f_m$ in Fig. 9 (e) while for other distances of L_{xp}, the sub-images are mostly non-circular [refer to Fig. 9 (f)]. Additionally, the non-circular sub-images have different shapes (i. e., the orientation of circular arcs) [refer to Fig. 9 (d)] and numbers with different L_{xp}. Macroscopically, in each flame image, the direction of the circular arcs of the non-circular sub-images is either toward the center of the flame [i. e., inward, refer to Fig. 9 (d)] or toward the edge of the flame [outward, refer to Fig. 9 (f)]. For $L_{xp} <= f_m$ [Fig. 9 (a)-(d)], the direction of the circular arcs is inward while for $L_{xp} > f_m$ [Fig. 9 (f)-(i)], the direction is outward. The number of the non-circular sub-images increases when L_{xp} became closer to the f_m, and yet reaches the least at $L_{xp} = 1.0 f_m$.

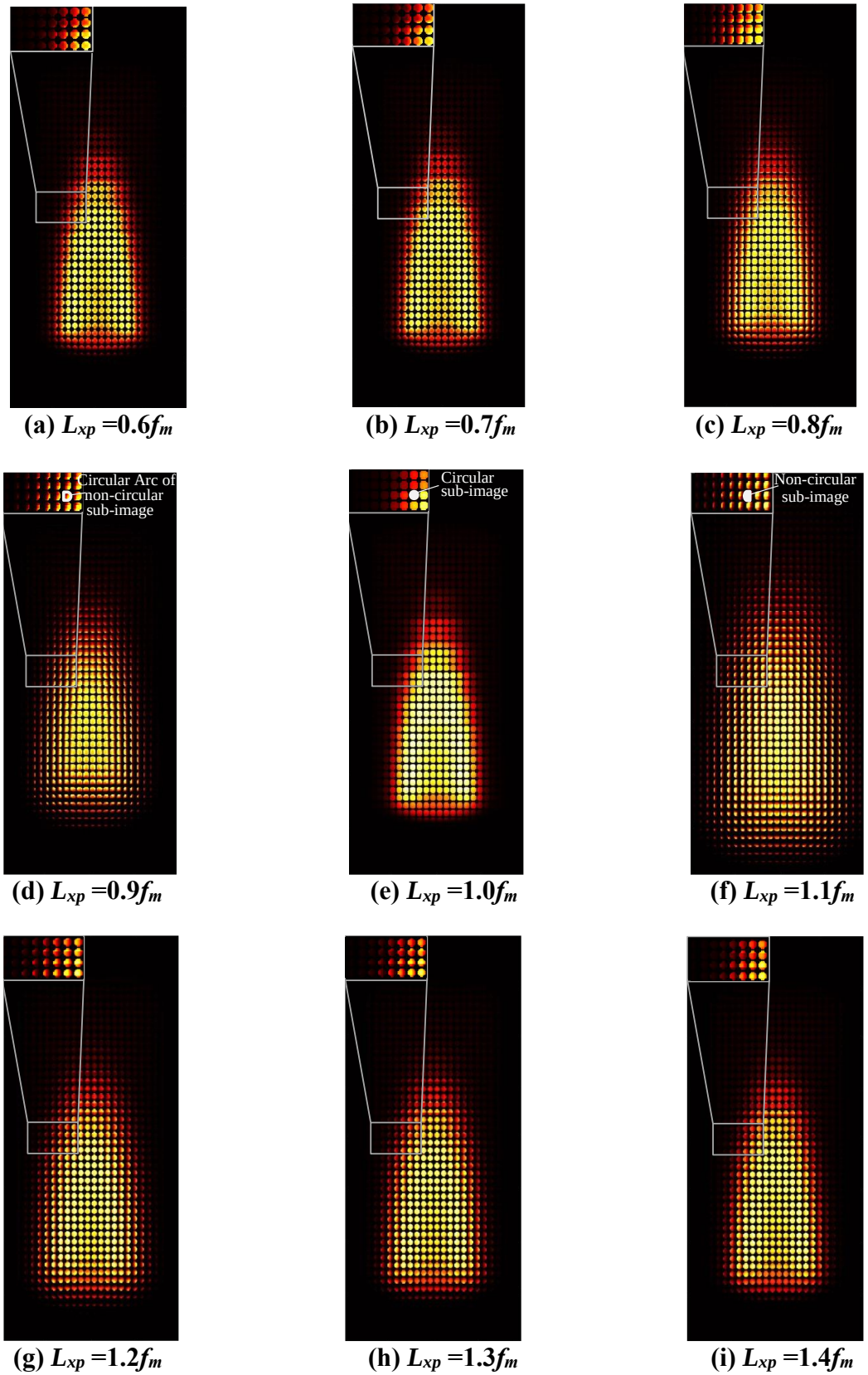

(a) L_{xp} =0.6f_m (b) L_{xp} =0.7f_m (c) L_{xp} =0.8f_m

(d) L_{xp} =0.9f_m (e) L_{xp} =1.0f_m (f) L_{xp} =1.1f_m

(g) L_{xp} =1.2f_m (h) L_{xp} =1.3f_m (i) L_{xp} =1.4f_m

Fig. 9 Simulated flame images with the different distances of L_{xp} for T_2.

Further to illustrate the non-circular and circular sub-images in the edge of the flame, the schematic of the sampled rays with different L_{xp} is drawn and shown in Fig. 10. In the figure, for the sub-image, the sampled rays of two boundary pixels are plotted to illustrate how the sampled rays crossed the flame cross-section. The representative sampled rays (marked by red lines) crossed the flame cross-section indicate that the flame radiation is sampled of the pixels. So, the corresponding pixels on the photosensor are appeared as bright (marked red). When the representative sampled rays are originated from outside the flame cross-section, no flame radiation is received by the pixels. The representative sampled rays (red lines or grey lines) are presented according to the conjugate relations in each type of light field camera. In Fig. 10, the conjugate relations in the light field cameras are expressed as follows, the conjugate points are in the same chief ray (dashed lines cross the lens center) and marked in the same color (black or blue) and the grey polygons denote the imaging beam of rays from one point to its conjugate point. It is clearly seen that the different distances of L_{xp} correspond to the different conjugate relations and different crossings between the sampled rays with the flame cross-section. This results in the differences in shape and a number of non-circular sub-images with the different L_{xp}.

It can be seen that two boundary pixels in the sub-images sampled the flame radiation [Fig. 10 (b)] at $L_{xp} = 1.0f_m$ and so all the pixels in the sub-image received the flame radiation. As a result, the sub-image is circular (red circle). For the $L_{xp} < f_m$, the pixels are close to the flame center can sample the flame radiation while the pixels are far away from the flame center cannot receive the flame radiation [Fig. 10 (a)]. Nevertheless, for the $L_{xp} > f_m$, the sampling characteristics of the pixels in the sub-images are opposite [Fig. 10 (c)]. Due to this the sub-images on the photosensor are not completely circular and have opposite orientations in the two cases [($L_{xp} < f_m$) and ($L_{xp} > f_m$)] on the edge of the flame. In the sub-image, the circular sub-images indicate that the sampled radiation of the pixels is from the same point inside the flame compared to the non-circular sub-images. For the same source point, lower sampled information can be achieved in comparison to different source points. For the traditional light field camera, the sampled radiation information of the pixels is close to each other in the circular sub-images, and the sampled radiation information is less than that of the focused light field camera. This less sampled radiation information is disadvantageous for the flame temperature reconstruction.

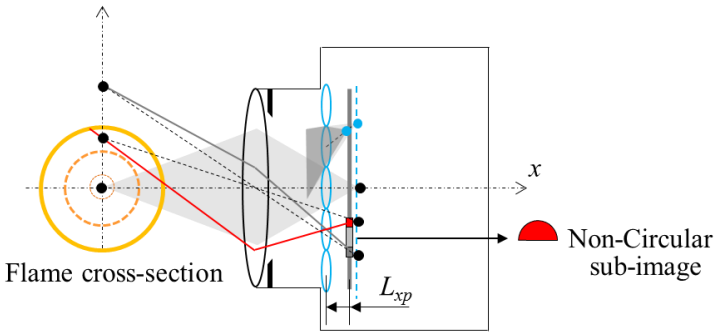

(a) $L_{xp} < f_m$

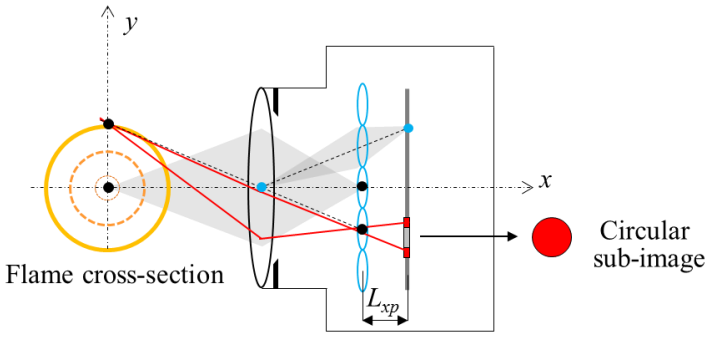

(b) $L_{xp} = f_m$

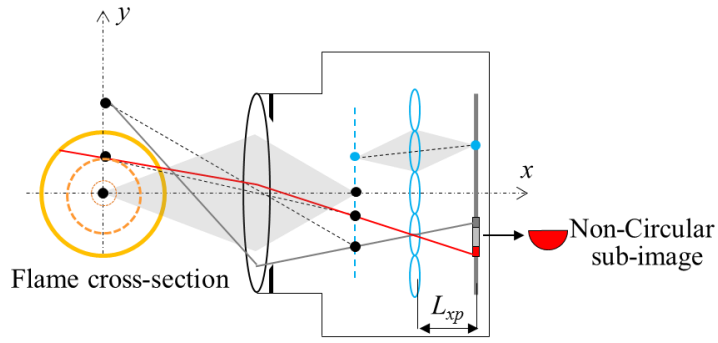

(c) $L_{xp} > f_m$

Fig. 10. Schematic of the sampled rays of the pixels in the sub-image under different L_{xp}.

4.2 Results of simulated flame

Based on the above discussion, it is clearly shown that the different light field cameras have different sampling characteristics of the flame radiation. Therefore, it is crucial to investigate the performance of the different light field cameras for the flame temperature reconstruction. The flame temperature is reconstructed for different light field cameras with different distances of L_{xp} using the NNLS algorithm. The relative errors Δ_T of the reconstructed temperature of each voxel are then calculated for the different distances of L_{xp}. The maximum and mean relative errors Δ_T are also obtained from all flame voxels and shown in Fig.11. It indicates that the reconstruction error increases with the decrease of the *SNR* value. For the maximum relative error, the highest value is observed about 15.76% for the *SNR* = 15dB and the highest mean relative error is 3.44% for the *SNR* = 15dB.

As discussed in Sections 2.2 and 2.3, the focused light field camera at L_{xp}=1.4f_m has more accurate sampled rays of each pixel and the representative sampled rays are more uniform at L_{xp} =1.4f_m. Hence, the focused light field camera at L_{xp}=1.4f_m should have least error of Δ_T. Instead, the lowest relative errors [maximum: 5.97% and 8.97% for *SNR* = 20dB and 15dB respectively), mean: 0.95% and 1.85% for *SNR* = 20dB and 15dB, respectively)] have been observed at the distance of L_{xp}= 0.7f_m. In addition, variations of the Δ_T have also been seen at different *SNR*s for the focused light field cameras. This indicates that temperature reconstruction of the flame with a focused light field camera ($L_{xp} > f_m$ and $L_{xp} < f_m$) is not sensitive to the sampling characteristics of the flame radiation caused by the L_{xp}. For each *SNR*, it is also clearly shown that the error Δ_T is greater at L_{xp} = 1.0f_m than the other distances of L_{xp}. This is due to fact that the less effective sampled radiation information obtained by the traditional light field camera as discussed in Sections 2.3 and 4.1.

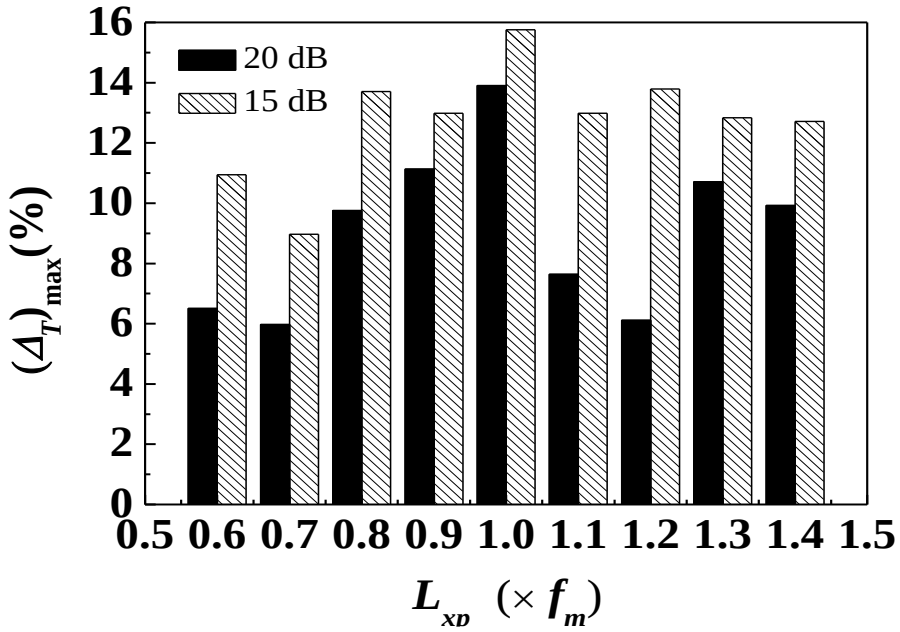

(a) The maximum relative error

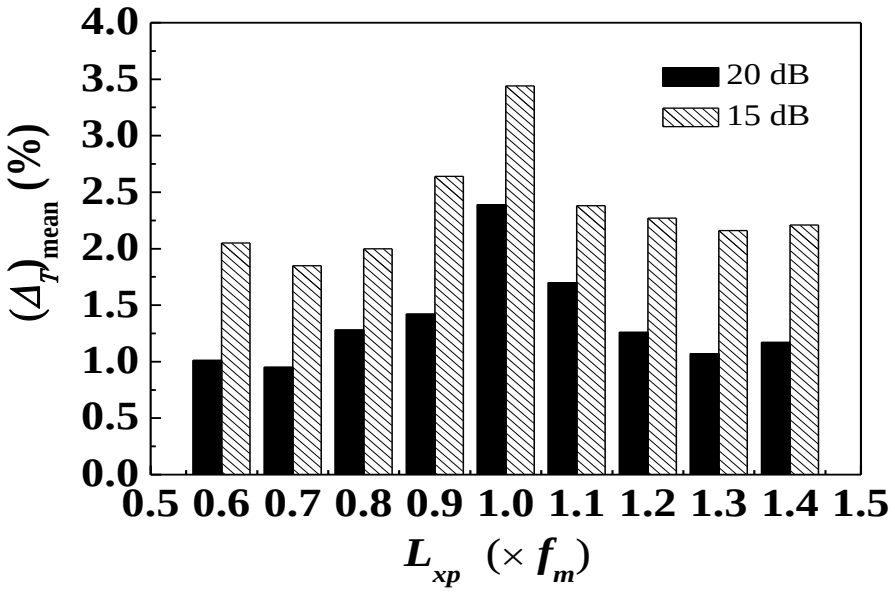

(b) The mean relative error

Fig. 11. The relative error of the reconstructed temperature of different light field cameras.

It has been realized that the relative errors of the flame voxels are insufficient to describe the reconstruction results and to conclude which light field camera is better for the flame temperature measurement. So further to verify the performance of the light field cameras, the temperature distribution of

the flame voxels are presented and described. Figure. 12 shows the reconstructed temperature distribution and the relative errors over the flame longitudinal sections with the different distances of L_{xp}. It has been observed that the flame temperature is reconstructed less accurately for the *SNR* = 15dB in comparison to the *SNR* = 20dB. Similar results are also found for the different *SNR*s with different $L_{xp.}$ For each *SNR*, the distributions of the reconstructed temperature of the focused light field camera ($L_{xp} > f_m$ and $L_{xp} < f_m$) are very similar to each other, as shown in Fig 12 (b) - (c). It further illustrates that for the focused light field camera, the reconstruction accuracy of the flame temperature is insensitive to the sampling characteristics of the flame radiation caused by the L_{xp}.

It has been found that the traditional light field camera has less sampling angle (*SA*) than the focused light field camera at $L_{xp} < f_m$ [Fig. 5 (b)]. It means that the traditional light field camera has the more accurate direction of sampled rays of each pixel than the focused light field camera at $L_{xp} < f_m$. In this case, the traditional light field camera should perform better than the focused light field camera at $L_{xp} < f_m$. However, since the traditional light field camera provides non-uniform representative sampled rays, it is obviously shown that the temperature is reconstructed poorly than the focused light field camera ($L_{xp} < f_m$) for the each *SNR*. Therefore, it indicates that the flame temperature measurement with a traditional light field camera is more sensitive to the uniformity of the representative sampled rays than the accuracy of the sampled rays' direction of each pixel. Finally, the results obtained from the numerical simulation suggested that the focused light field camera performed better for the flame temperature measurement compared to the traditional light field camera.

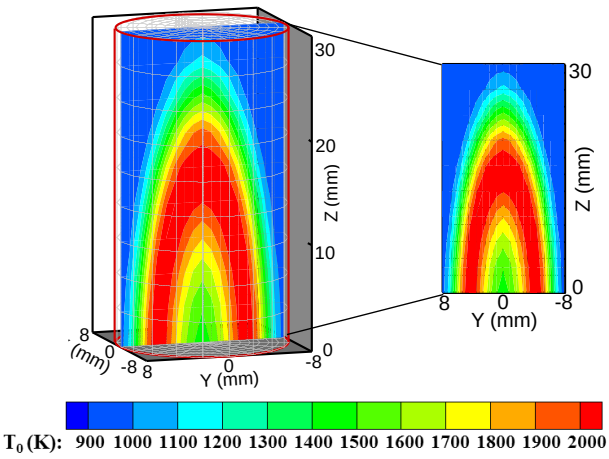

(a) The axisymmetric true temperature distribution of the simulated flame (T_0)

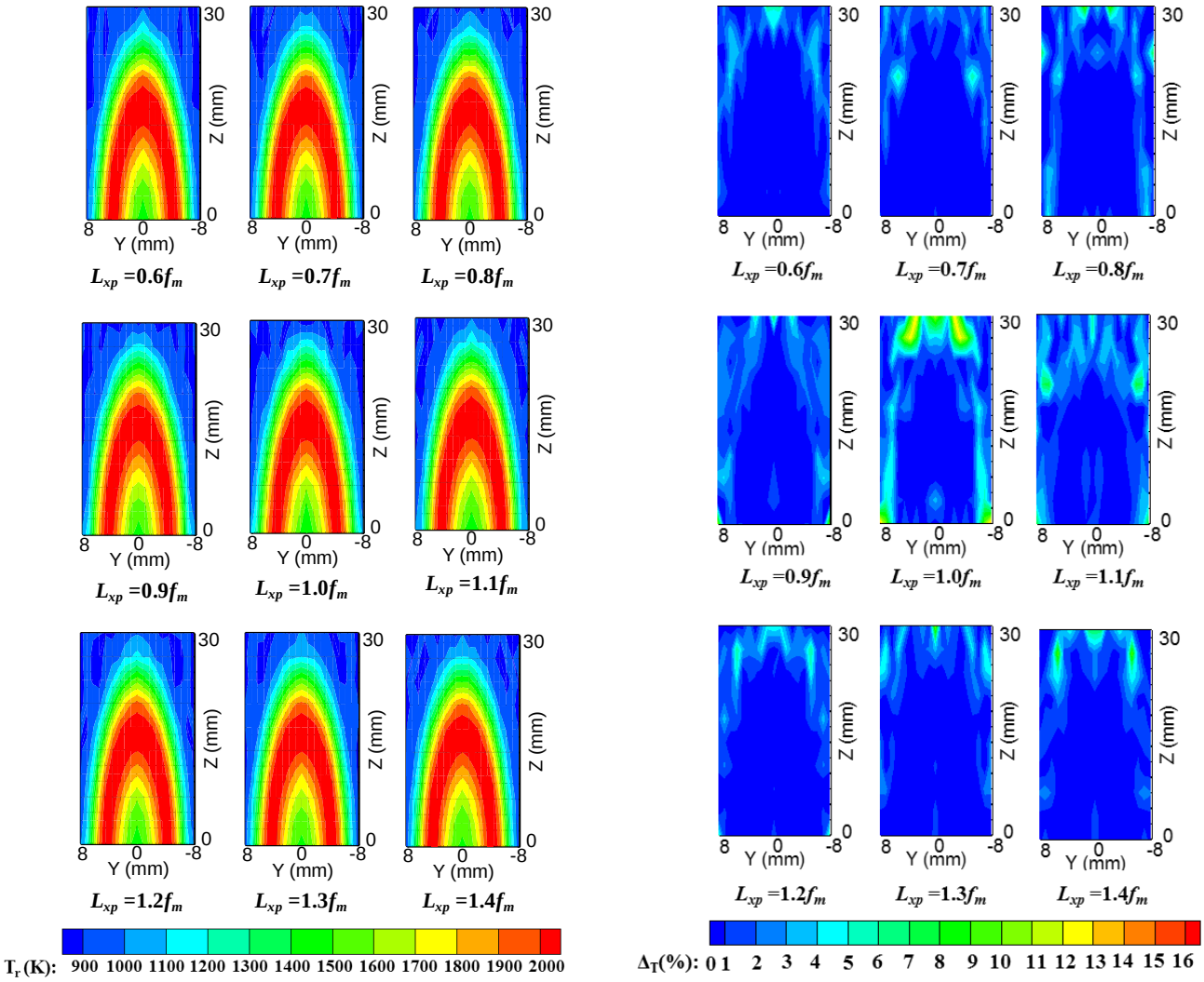

(b) The reconstructed temperature, *SNR*=20 dB **(c) The relative errors, *SNR* = 20 dB**

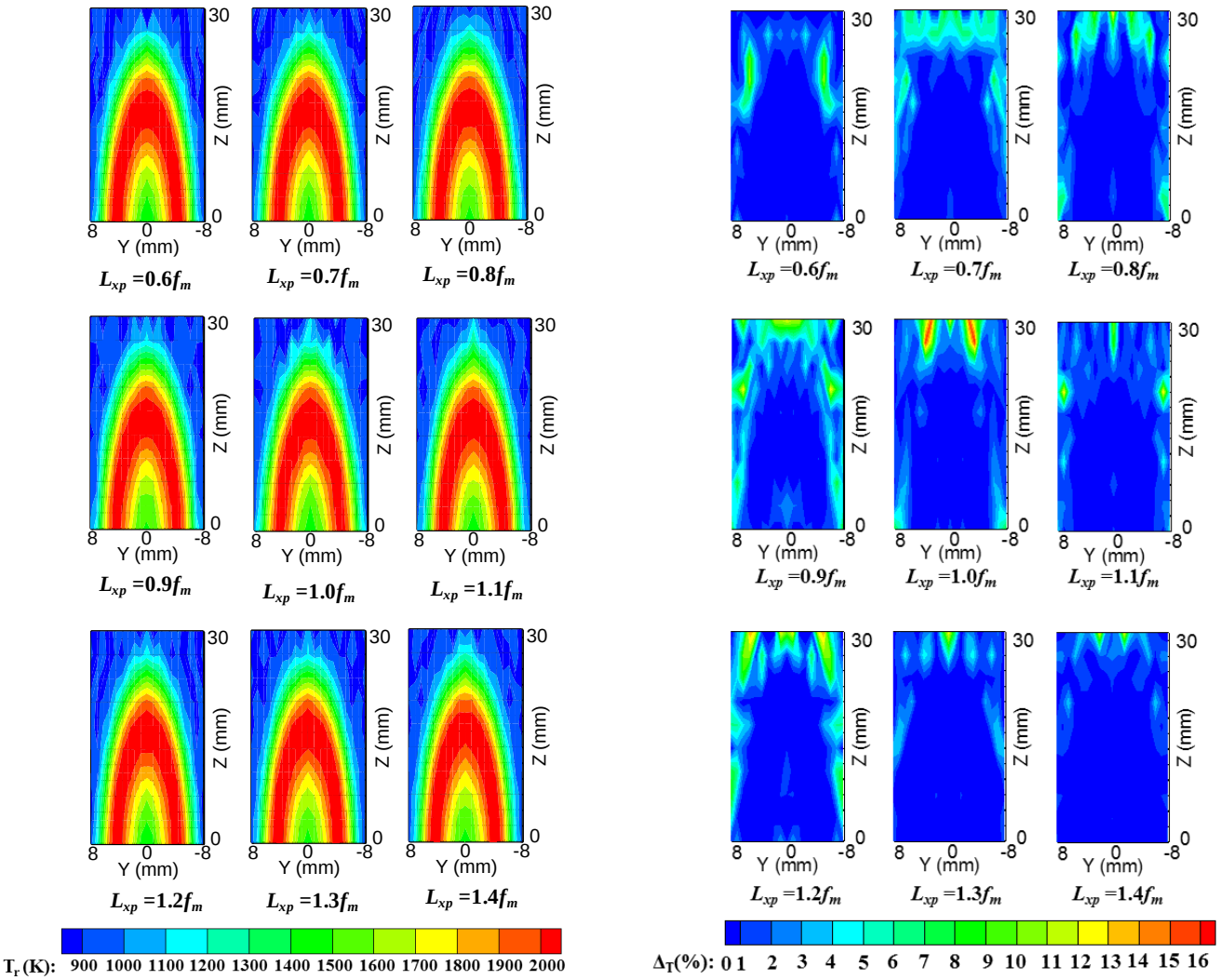

(d) The reconstructed temperature, *SNR*=15 dB **(e) The relative errors, *SNR* =15 dB**

Fig. 12. The reconstructed temperature and relative error distributions over a longitudinal section of the cylindrical flame with different distances of L_{xp}.

5. Experimental research

To validate the proposed NNLS algorithm, experiments were carried out to reconstruct the temperature distribution of ethylene diffusion flames based on the light field imaging. The experimental setup is shown in Fig. 13. In this figure, the combustion supporting components are used to supply the compressed air and ethylene (C_2H_4) to the burner. The burner is comprised of an inner tube (12 mm) for fuel (ethylene) flow and an external tube (50 mm) for air flow [5], as shown in Fig. 14. The co-flow of air is used to stabilize the fuel flow in the inner tube for the steady flame. A focused light field

camera (Raytrix, R29, the number of the microlenses of the microlens array is 207×160) is placed inside a shield to avoid the hot environment and the light field camera is used to capture the flame images. The light field flame images are captured under three different combustion operating conditions [40] which are shown in Table. 2. In the table, air to fuel equivalence ratio (AFER) is defined as the ratio of the actual air/fuel ratio to the stoichiometric air/fuel ratio.

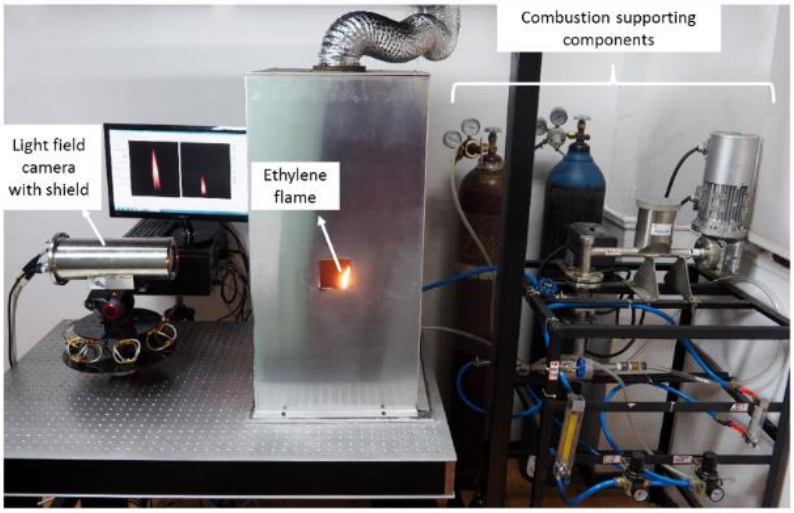

Fig. 13. Experimental setup of flame temperature measurement using the focused light field camera.

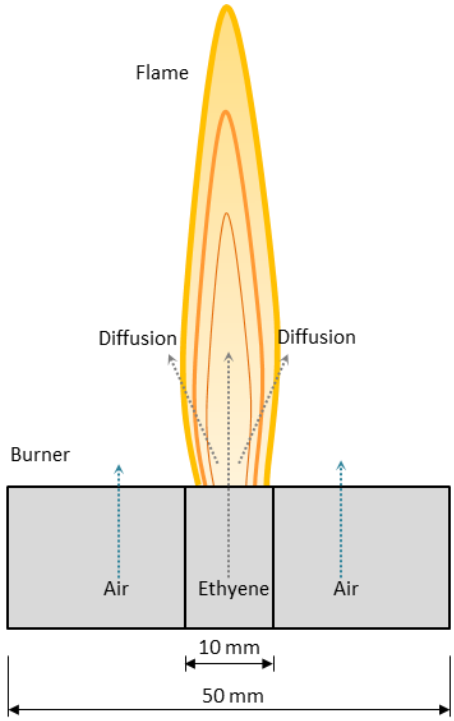

Fig. 14. Schematic of the co-flow burner.

Table 2. Operating conditions

Condition	AFER	Air (mL/s)	C_2H_4 (mL/s)	Oxygen content (%)
1	11.1	713.3	4.60	21
2	13.2	713.3	3.85	21
3	22.2	713.3	2.30	21

Figure 15 shows the flame images captured under the three different conditions and the reconstructed temperature distributions of the ethylene diffusion flames using the proposed NNLS algorithm described in Section 3. It has been observed that the height of the flame becomes smaller when the AFER is increased due to the lower ethylene flow rate from condition 1 to condition 3. It can be seen that the flame temperature varies from 800 K - 1950 K for those conditions. For each condition, it can

be seen that the flame temperature increases and then decreases along the diffusion path (i.e., from the outlet of the burner to the surroundings, refer to Fig. 14) of the fuel.

Experimental results have also shown agreement with the results obtained by the Ref. [39]. It has been observed that the peak temperatures of the flame are about 100K- 150K lower in comparison to Ref. [39]. Since the empirical constant absorption coefficient (3 m^{-1}) is used in this study [36, 37] and in reality is not constant for the realistic flames, which can lead to some measurement errors. The measurement errors can also be caused by other factors such as geometric calibration error, the error of mathematical model caused by ignoring scattering inside the flame. The geometric calibration error is investigated in details in our previous research [41]. To eliminate the error of considering constant absorption coefficient, further research will focus on the simultaneous reconstruction of the absorption coefficient and temperature. Finally, the results obtained from the experiments suggested that the proposed NNLS algorithm has proved to be applicable for the realistic flame to reconstruct the temperature distributions.

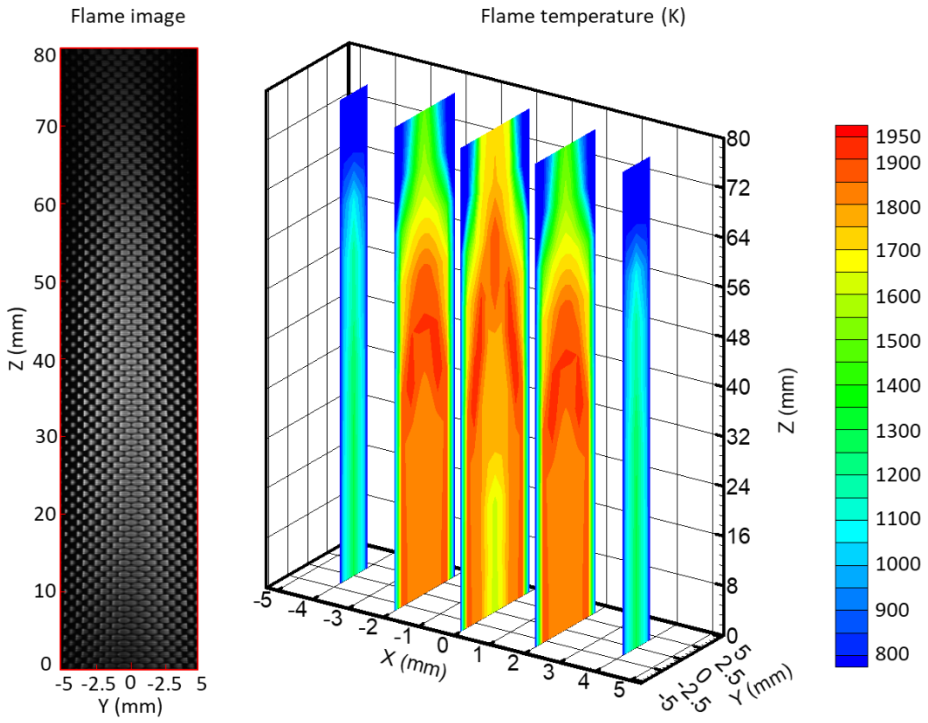

(a) Condition 1

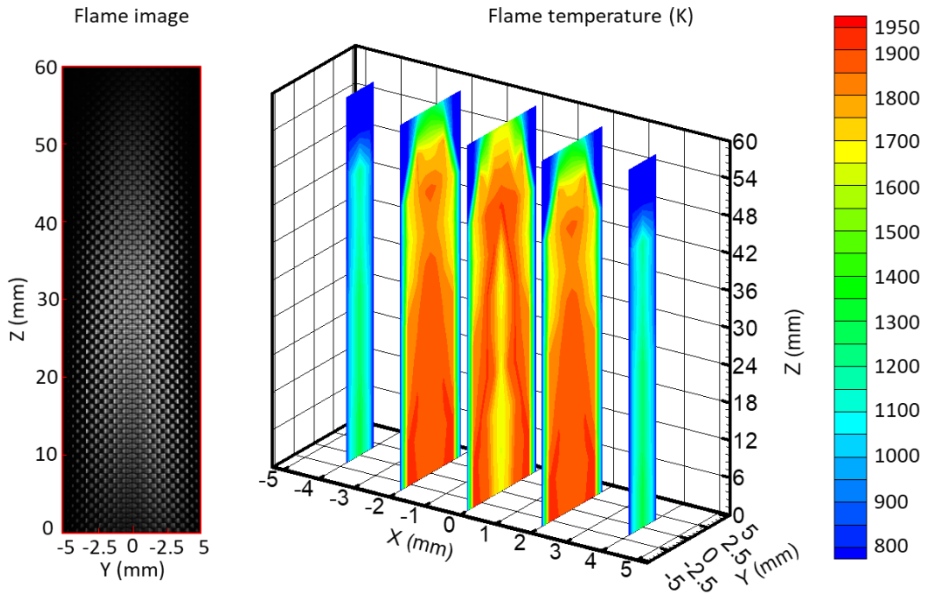

(b) Condition 2

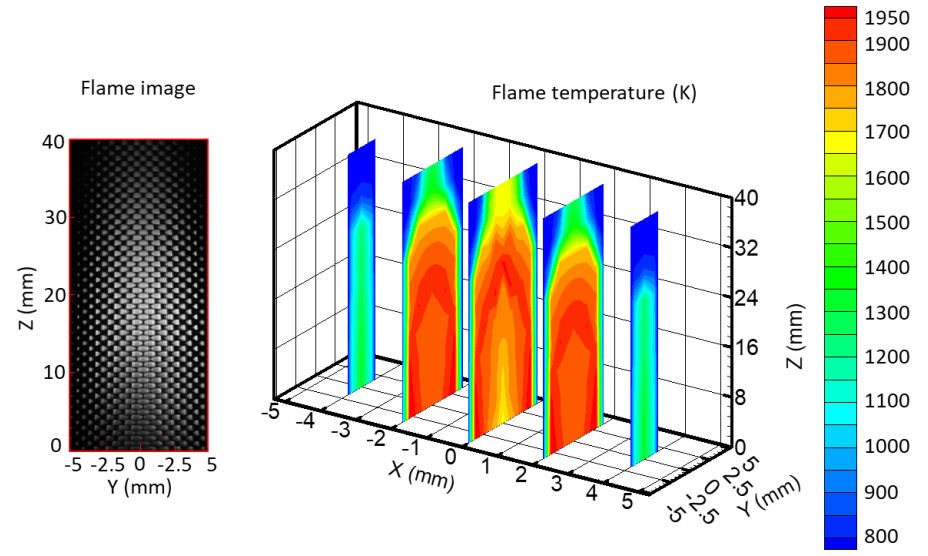

(c) Condition 3

Fig. 15. The reconstructed temperature distributions over five longitude-sections of ethylene diffusion flames.

6. Conclusions

In this paper, the effects of radiation sampling of the different light field cameras have been investigated for the flame temperature reconstruction. Numerical simulations were carried out to investigate the reconstruction accuracy of the flame temperature. The sampling region and sampling angle of the light field cameras have been defined to evaluate the number of sampled rays and the directional accuracy of the sampled rays for each pixel. A representative sampled ray is considered to illustrate all the sampled rays of each pixel and to determine the direction of the flame radiation. The uniformity of the representative sampled rays has been presented and analyzed. A non-negative least square (NNLS) algorithm was used to reconstruct the temperature distribution of simulated and experimental flames. The concluding remarks obtained from the numerical simulations are summarized as follows;

(1) It has been found that the focused light field camera at the distance of $1.4\times f_m$ has the lowest sampling angle and thus least number of sampled rays of each pixel. The sampled rays of each pixel can approach more accurately from a single direction in comparison to the traditional light field camera and it is useful for the flame temperature reconstruction.

(2) The traditional light field camera has the least uniform representative sampled rays than the focused light field cameras. It has also been observed that in the circular sub-image, the sampled radiation of the pixels is closer to each other compared to the focused light field camera and it can sample the radiation information less effectively than the focused light field camera.

(3) The relative errors obtained from the reconstruction are 2.39% and 3.44% respectively for the signal-to-noise ratios of 15dB and 20dB. It has been illustrated that for each signal-to-noise ratio, the relative error is higher for the traditional light field camera than the focused light field camera. The distribution of the temperature reconstruction is also better for the focused light field camera.

(4) For the focused light field camera, the results suggested that the reconstruction accuracy of the flame temperature is insensitive to the characteristics of the radiation sampling caused by distances from microlens array to the photosensor. It also indicates that the reconstruction accuracy of the flame with the light field camera mostly depends on the uniformity of the representative sampled rays than the directional accuracy of the sampled rays of each pixel.

(5) Experimental results indicated that the proposed reconstruction model is applicable for reconstructing the temperature distributions of practical flames.

Further study will focus on the effects of radiation sampling of the different light field cameras with non-axisymmetric true temperature distribution. The effects of different absorption and scattering coefficients will also be investigated for the flame temperature reconstruction.

Acknowledgements and Funding

This work was supported by the National Natural Science Foundation of China [grant numbers 51676044, 51506030, 51327803]; Natural Science Foundation of Jiangsu Province for Distinguished Young Scholars [grant number, BK20150023]; Scientific Research Foundation of Graduate School of Southeast University [grant number, YBJJ1605].

References

1. J. Doi and S. Sato, "Three-dimensional modeling of the instantaneous temperature distribution in a turbulent flame using a multidirectional interferometer," Opt. Eng. **46**(1), 015601-1-015601-7 (2007).
2. L. Ma, W. Cai, A.W. Caswell, T. Kraetschmer, S. T. Sanders, S. Roy, and J. R. Gord, "Tomographic imaging of temperature and chemical species based on hyperspectral absorption spectroscopy," Opt. Express **17**(10), 8602-8613 (2009).
3. M. M. Hossain, G. Lu, and Y. Yan, "Optical fiber imaging based tomographic reconstruction of burner flames. *IEEE Transactions on Instrumentation and Measurement*," **61**(5), 1417-1425 (2012).
4. M. Levoy and P. Hanrahan, "Light field rendering," in *Proceedings of the 23rd annual conference on Computer graphics and interactive techniques*, (ACM, 1996), pp. 31-42.
5. J. Sun, C. Xu, B. Zhang, M. M. Hossain, S. Wang, Hong Qi, and H. Tan, "Three-dimensional temperature field measurement of flame using a single light field camera," Opt. Express **24**(2), 1118-1132 (2016).
6. R. Ng, M. Levoy, M. Brédif, G. Duval, M. Horowitz, and P. Hanrahan, "Light field photography with a hand-held plenoptic camera," Computer Science Technical Report CSTR of Stanford University, 1-11 (2005).
7. T. Georgiev, Z. Yu, A. Lumsdainec, and S. Goma, "Lytro camera technology: theory, algorithms, performance analysis," Proc. SPIE-IS&T Electronic Imaging **8667**, 86671J-1-86671J-10 (2013).
8. C. L. Tien and S. C. Lee, "Flame radiation," Prog. Energy Combust. Sci. **8**(1), 41-59 (1982).

9. T. G. Georgiev and A. Lumsdaine, "Resolution in Plenoptic Cameras," in *Computational Optical Sensing and Imaging Conference*, OSA Technical Digest (CD) (Optical Society of America, 2009), paper CTuB3.
10. W. Cai, X. Li, F. Li, and L. Ma, "Numerical and experimental validation of a three-dimensional combustion diagnostic based on tomographic chemiluminescence," Opt. Express **21**(6), 7050-7064 (2013).
11. Q. Lei, Y. Wu, W. Xu, and L. Ma, "Development and validation of a reconstruction algorithm for three-dimensional nonlinear tomography problems," Opt. Express **24**(14), 15912-15926 (2016).
12. H. N. Yang, B. Yang, X. S. CAI, C. Hecht, T. Dreier, and C. Schulz, "Three-dimensional (3-D) temperature measurement in a low pressure flame reactor using multiplexed tunable diode laser absorption spectroscopy (TDLAS)," Laser. Eng. **31**, 285-297 (2015).
13. L. An, R. Wang, and G. Shen, "Overview of Furnace Three-Dimensional Temperature Field Reconstruction Algorithms Based on Acoustic Theory," Power Syst. Eng. **30** (5), 9-12 (2014).
14. P. M. Brisley, G. Lu, Y. Yan, and S.Cornwell, "Three-dimensional temperature measurement of combustion flames using a single monochromatic CCD camera," IEEE Trans. Instrum. Meas. **54**(4), 1417-1421 (2005).
15. M. M. Hossain, G. Lu, D. Sun, and Y. Yan, "Three-dimensional reconstruction of flame temperature and emissivity distribution using optical tomographic and two-color pyrometric techniques," Meas. Sci. Technol **24**(7), 1-10 (2013).
16. D. Liu, J. Yan, and K. Cen. "On the treatment of non-optimal regularization parameter influence on temperature distribution reconstruction accuracy in participating medium," Int. J. Heat Mass Transfer, **55**(5–6), 1553-1560 (2012).
17. D. Liu, F. Wang, J. H. Yan, Q. X. Huang, Y. Chi, and K. F. Cen, "Inverse radiation problem of temperature field in three-dimensional rectangular enclosure containing inhomogeneous, anisotropically scattering media" Int. J. Heat Mass Transfer, **51**, 3434-3441(2008).
18. C. Xu, W. Zhao, J. Hu, B. Zhang, and S. Wang, "Liquid lens-based optical sectioning tomography for three-dimensional flame temperature measurement," Fuel **196**, 550-563 (2017).
19. C. Niu, H. Qi, X. Huang, L. Ruan, W. Wang, and H. Tan, "Simultaneous reconstruction of temperature distribution and radiative properties in participating media using a hybrid LSQR-PSO algorithm," Chinese Phys. B **24**(11), 114401-1- 114401-11 (2015).
20. C. Lou, W. H. Li, H. C. Zhou, and C. T. Salinas, "Experimental investigation on simultaneous measurement of temperature distributions and radiative properties in an oil-fired tunnel furnace by radiation analysis," Int. J. Heat Mass Transfer, **54**, 1-8 (2011).

21. H. Zhou, S. Han, F. Sheng, and C. Zheng. "Visualization of three-dimensional temperature distributions in a large-scale furnace via regularized reconstruction from radiative energy images: numerical studies," J. Quant. Spectrosc. Radiat. Transfer **72(**4), 361-383 (2002).
22. K. C. Lück, and F. J. Müller. "Simultaneous determination of temperature and OH-concentration in flames using high-resolution laser-absorption spectroscopy," J. Quant. Spectrosc. Radiat. Transfer **17**(3), 403-409 (1977).
23. H. Zhao, B. Williams, and R. Stone. "Measurement of the spatially distributed temperature and soot loadings in a laminar diffusion flame using a Cone-Beam Tomography technique," J. Quant. Spectrosc. Radiat. Transfer 133, 136-152(2014).
24. C. Niu, H. Qi, X. Huang, L. Ruan, and H.Tan, "Efficient and robust method for simultaneous reconstruction of the temperature distribution and radiative properties in absorbing, emitting, and scattering media," J. Quant. Spectrosc. Radiat. Transfer **184**, 44-57 (2016).
25. R. Raghavendra, K. B. Raja, and C. Busch, "Presentation attack detection for face recognition using light field camera," IEEE Trans. Image Process. **24**(3), 1060-1075 (2015).
26. T. Li, S. Li, S. Li, Y. Yuan, and H. Tan, "Correction model for microlens array assembly error in light field camera," Opt. Express **24**(21), 24524-24543 (2016).
27. Y. Endo, K. Wakunami, T. Shimobaba, T. Kakue, D. Arai, Ya. Ichihashi, K. Yamamoto, and Tomoyoshi, "Computer-generated hologram calculation for real scenes using a commercial portable plenoptic camera," Opt. Commun. **356**, 468-471 (2015).
28. M. Goulet, M. Rilling, L. Gingras, S. Beddar, L. Beaulieu, and L. Archambaulta, "Novel, full 3D scintillation dosimetry using a static plenoptic camera," Med. Phys. **41**(8), 082101-1-082101-13 (2014).
29. Y. Yuan, B. Liu, S. Li, and H. Tan, "Light-field-camera imaging simulation of participatory media using Monte Carlo method," Int. J. Heat Mass Transfer **102**, 518-527 (2016).
30. T. Georgiev and A. Lumsdaine, "Focused plenoptic camera and rendering," J. Electron. Imaging **19**(2), 021106-01-021106-11 (2010).
31. A. Lumsdaine and T. Georgiev, "The focused plenoptic camera," in *Proceedings of IEEE International Conference on Computational Photography* (IEEE, 2009), pp. 1-8.
32. A. Lumsdaine, T. Georgiev, and G. Chunev, "Spatial analysis of discrete plenoptic sampling," Electronic Imaging. Proc. SPIE-IS&T Electronic Imaging **8299**, 829909-1-829909-10 (2012).
33. C. L. Lawson and R. J. Hanson, Solving least squares problems, (Prentice-Hall, 1974).
34. T. Georgiev and A. Lumsdaine, "Depth of field in plenoptic cameras," in *Proceedings of Eurographics*, (2009), pp. 1-4.

35. P. Lin, New Computation Methods for Geometrical Optics, (Springer, 2014).
36. X. Huang, H. Qi, C. Niu, L. Ruan, H. Tan, J. Sun, and C. Xu, "Simultaneous reconstruction of 3D temperature distribution and radiative properties of participating media based on the multi-spectral light-field imaging technique," Applied Thermal Engineering, **115**, 1337-1347 (2017).
37. H. Liu, S. Zheng, and H. Zhou, "Measurement of soot temperature and volume fraction of axisymmetric ethylene laminar flames using hyperspectral tomography," IEEE Transactions on Instrumentation & Measurement, **66**(2), 315-324 (2016).
38. J. Felske and C. Tien, "Calculation of the emissivity of luminous flames," Combust. Sci. Technol. **7**(1), 25-31 (1973).
39. L. Boltzmann, "Ableitung des Stefan'schen Gesetzes, betreffend die Abhängigkeit der Wärmestrahlung von der Temperatur aus der electromagnetischen Lichttheorie," Annalen der Physik **258**(6), 291-294 (1884).
40. R. J. Santoro, T. T. Yeh, J. J. Horvath, and H. G. Semerjian, "The transport and growth of soot particles in laminar diffusion flames," Combustion Science & Technology, **53**(2-3), 89-115 (1987).
41. J. Sun, M. M. Hossain, C. L. Xu, B. Zhang, and S. M. Wang, "A novel calibration method of focused light field camera for 3-d reconstruction of flame temperature," Optics Communications, 390, 7-15 (2017).